

Extending the reach of single-chamber inflatable soft robots using Magnetorheological Fluids

J. Garrett Williamson¹, Caroline Schell², Michael Keller³, and Joshua Schultz⁴

Abstract—Elastomer based, fabric-reinforced, inflatable soft robots bend when inflated because the fabric-reinforced section has negligible strain compared to the unreinforced section. The inherent displacement mismatch will cause the robot to stretch in the manner of a bi-metallic strip. Using a similar principle, we alter the inflation-dependent motion of various fabric reinforced soft robots by changing the stiffness of different regions of their chamber walls. A concatenated workspace volume of these many robots presents an increase in volume by a factor of six when compared to a robot of uniform rubber composition. A finite element method for a magnetically responsive truss demonstrates an increase in stiffness twofold from a magnetic field strength of 0.01 Tesla to a field strength of 0.02 Tesla. It is postulated that by utilizing these magnetically activated truss configurations as channels within silicone rubber, a fabric-reinforced robot will be able to move about a workspace of similar size by varying magnetic field strength along with the inflation pressure.

I. INTRODUCTION

Soft robots show great promise for performing tasks in a manner quite different from traditional robots, but achieving the desired motions has proved to have many technical challenges. Attempts to create truly dexterous soft robots with 3-dimensional workspaces often result in complex networks of chambers and valves [1]–[4]. While not without success, these complicated systems have some downsides. Intricate, multi-chambered robot bodies with these complicated supply and control networks have some downsides. They must be either tethered by pneumatic tubes or have self-contained supply and control modules, which are usually rigid.

Nature utilizes a more simple and elegant solution than these multi-chambered robots. The sea pig (*scotoplanes globosa*) moves itself by inflating single-chambered legs [5]. Mimicking this, the goal of this work is to demonstrate that complex movement can be achieved by varying the wall stiffness of a single-chamber. An inflatable soft robot arm with sections that are stiffer will deform non-uniformly when inflated. This is because the stiffer patches will undergo smaller strains than the more compliant regions. The body will deform around the stiff patch allowing the robot to reach about its environment when inflated, rather than following a single inflation-displacement curve. We plan to realize this varying of wall stiffness by exploiting the increase in apparent viscosity of magnetorheological fluid when exposed to a magnetic field. When the location and strength of this

magnetic field is varied, the stiffness of different sections on the robot arm will also vary, inducing motion.

The motion caused by the magnetorheological induced wall stiffening will modify a default arm motion. This overall motion is built into the geometry of the created arm by incorporating an inelastic strip of textile into the wall of that arm, as other research has done previously [6]. As the chosen geometry is curved, a fabric with a radial weave was chosen (Figure 1). While various incarnations of fabric-reinforced inflatable soft robots have been presented in recent years, the manner in which each moves is governed only by the geometry of the unreinforced sections of the chamber as it inflates. To the authors' knowledge, there is no work that rapidly modifies the elastic properties of the chamber wall at run-time to direct the movement. We begin to explore this idea in this paper by examining the ability of the channels filled with magnetorheological fluids to modulate the stiffness, and the resulting kinematic behavior by comparing multiple robots, each with the different elastic properties we expect would result from varying the magnetic field.

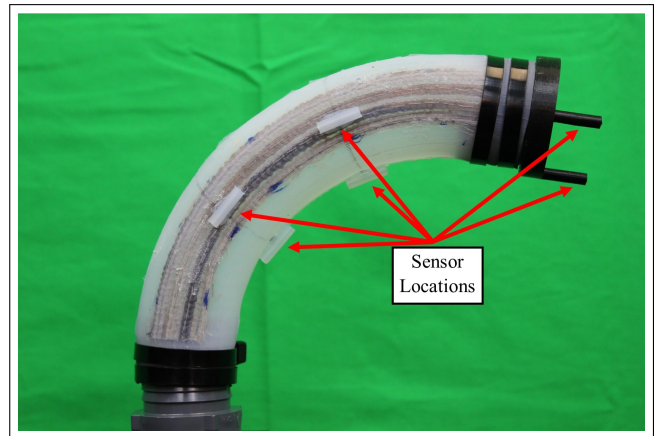


Fig. 1: Arm Geometry

II. MODELING MAGNETO-MECHANICAL BEHAVIOR

Smart materials allow for a dynamic, tunable, stiffness in a soft robot, increasing the movement envelope. Local changes in material stiffness change the deformation response of the soft robot. Typical pneumatically actuated soft robots may be designed to inflate separate chambers with air at differing pressures to induce different poses. The multi-chambered soft robots have a workspace constrained by the network of chambers and the pneumatic actuation lacks a tunable stiffness. Several approaches have been adopted to modify

Funded by the NSF through EFRI grant 1935312

^{1,2,3,4}All authors are with the Department of Mechanical Engineering at The University of Tulsa, Tulsa, OK, USA
jgw3642, cas317, michael-keller, and
joshua-schultz with domain @utulsa.edu

stiffness through the application of pressure, heat, electricity, or magnetic field. The introduction of fluids or electrical currents are categorized as active approaches. Alterations of the operating conditions, like the application of heat to wax to induce a phase change, are categorized as semi-active approaches and often prove to have slower response to changes in stiffness than active approaches [1], [4]. A phase change from solid to liquid in materials utilizing thermally activated materials like wax, decreases the viscosity of the fluid, decreasing the stiffness of the material. While this method provides large stiffness changes, wax has a prolonged time to solidification, on the order of a few minutes [7], which would result in a bandwidth too low for many robotic applications. Our approach is a modified semi-active method that induces a phase change within the material via application of magnetic field and optimizes design of the fluid network for stiffness.

Magnetorheological (MR) fluid is a suspension of micron-sized ferrous particles in a liquid. Without a magnetic field, the particles flow freely in the suspension fluid. In the field-off state, MR fluids have a low viscosity that increases with increasing shear rate. When a magnetic field is applied to MR fluid, the particles orient themselves into chains. The orientation of particles align along the field lines as the magnetic field strength is increased. More particles will align with increasing field strength and the MR fluid will reach magnetic saturation when the maximum allowable chains have formed. In this field-on state, MR fluid behaves as a solid or viscoelastic material due to the particle alignment. Until the saturation point, the apparent viscosity increases, and the fluid can be characterized akin to Bingham plastic models [8]. In one study, the increase up to the maximum viscosity is on the order of 1-3 seconds when a magnetic field is applied to the MR fluid and the steady-state viscosity occurred after a field strength of 0.3 T. When the field is turned off, a relaxation period occurs which takes 1-2 seconds [9]. A rapidly responding material is advantageous compared to a thermally activated material. Thermally activated materials have heating and cooling periods that are longer than the activation and deactivation of an MR fluid; minutes compared to a few seconds [7]. However, thermally induced stiffness modulating methods provide more change in stiffness than that of MR fluids [1], [10].

The bulk stiffness of a structure implementing MR fluid can be influenced by the architecture of the chamber containing the fluid. In 3-D, some micro-scale lattice structures like octo-truss unit cells, exhibit isotropic behavior as a result of cubic symmetry and so they have an unchanging stiffness with respect to unit cell density [11]. Thus, the chamber or channels of a soft robot body material can be designed to yield stiffness changes optimized by the inherent structure using finite element analysis.

Lattice-like 3-D structures made up of cuboctahedron unit cells infilled with MR fluid were analyzed in a previous study. The change in effective stiffness was confirmed to be largest with the magnetic field oriented parallel to the direction of applied force [9]. This study first used small

struts of the same dimensions as those in the lattice structures to determine the effective shear and Young's moduli. The compression and bending tests of the struts filled with MR fluid showed the directional dependence of magneto-mechanical behavior. Under compression, fields applied parallel to the compressive force will provide a larger change in stiffness than a field applied perpendicularly, even at higher magnetic field strengths. In cantilevered bending tests, fields applied parallel to the direction of deflection will similarly increase stiffness while no stiffening occurs with fields applied perpendicular to the applied force. Linear relationships were used to determine the effective stiffening moduli as the previous experiments carried out compression and bending tests on individual struts with magnetic fields below the saturation threshold (0.3 T) applied in the direction of maximum stiffening [9]. The relationships for a magnetically infused strut are

$$\frac{F}{L} = \frac{EA}{L}(T) + c \quad (1)$$

$$\frac{F}{L} = \frac{EI}{L^3}(T) + c \quad (2)$$

In equations (1) and (2), $\frac{F}{L}$ is the force per unit length; E , the modulus of elasticity; A , the cross-sectional area; L , the member length; I , the moment of inertia; T , the magnetic field strength; and c is the initial stiffness due to hydrostatic pressure.

Our approach aims to use truss structures infilled with MR fluid placed within the walls of the robot elastomeric body, exploiting the phase change upon magnetic field application to increase stiffness. The standard stiffness matrix for the finite element analysis of a truss was modified to capture Euler-Bernoulli beam bending; the full matrix is shown below in equation 3.

$\mathbf{K} =$

$$T \begin{pmatrix} \frac{EA}{L}c^2 & \frac{EA}{L}cs & -\frac{EA}{L}c^2 & -\frac{EA}{L}cs & \\ +\frac{12EI}{L^3}s^2 & -\frac{12EI}{L^3}cs & -\frac{6EI}{L^2}s & -\frac{12EI}{L^3}s^2 & +\frac{12EI}{L^3}cs & -\frac{6EI}{L^2}s \\ & \frac{EA}{L}s^2 & \frac{6EI}{L^2}c & -\frac{EA}{L}cs & -\frac{EA}{L}s^2 & \frac{6EI}{L^2}c \\ & +\frac{12EI}{L^3}c^2 & +\frac{12EI}{L^3}cs & -\frac{12EI}{L^3}cs & -\frac{12EI}{L^3}c^2 & \\ & & \frac{4EI}{L} & \frac{6EI}{L^2}s & -\frac{6EI}{L^2}c & \frac{2EI}{L} \\ & \text{SYM} & & \frac{EA}{L}c^2 & \frac{EA}{L}cs & \frac{6EI}{L^2}s \\ & & & +\frac{12EI}{L^3}s^2 & -\frac{12EI}{L^3}cs & \\ & & & & \frac{EA}{L}s^2 & -\frac{6EI}{L^2}c \\ & & & & +\frac{12EI}{L^3}c^2 & \\ & & & & & \frac{4EI}{L} \end{pmatrix} \quad (3)$$

In equation 3, T is the magnetic field strength measured in Tesla; s is $\sin \theta$; c , $\cos \theta$; θ , the angle measured counter-clockwise from the first element's coordinate to the truss element; A , the cross-sectional area; L , the member length; E , the modulus of elasticity; and I is the moment of inertia. Finite element analysis was used to model the behavior of a magnetically responsive truss in an elastomeric body. To

determine the range in which a chamber wall region impregnated with a magnetorheological truss could be stiffened, we analyzed a simple planar truss (seen in Figure 2) using FEA for different loading conditions and field strengths.

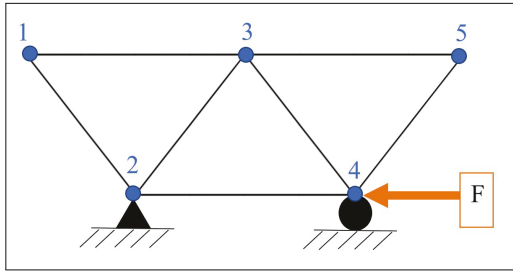


Fig. 2: Simple truss design with compressive loading at support node

In Matlab, the model uses user-defined truss attributes such as the number of nodes, members, imposed forces and nodal coordinates as well as material properties. Outputs of the model include nodal displacements, axial stresses, and support reactions. For a range of magnetic field strengths, the model builds the local stiffness matrix and local load vector of an element in the truss using the linear relationships described in equations (1) and (2). Then the reactions are transferred to matrices that store the applied loads and the imposed displacements. Following this, the global stiffness matrix is calculated and stored in separate arrays to distinguish between the prescribed and free degrees of freedom. The displacements are solved by taking the inverse of the applied load vector and multiplying it by the global stiffness matrix containing all the free degrees of freedom.

The truss structure simulated via FEA is shown in Figure 2. A force was applied to node 4 and the load-displacement response was determined by varying the applied load and calculating the displacement. Data from the lattice structure study [9] was used to calculate the effective shear and Young's moduli in simulations. Future experiments will utilize a similar hydrocarbon based MR fluid; Parker Lord MRF-122EG. The simulations ranged from no magnetic field application (0.0 T) up to the yield point or magnetic saturation of the fluid (0.2 T).

This model assumes that the application of the magnetic field is in the direction of maximal change in stiffening. This implies that the strut members of the truss are oriented such that the magnetic field lines are in the same direction as the compressive load. In the load vs. displacement curve the magnetic field increases from right to left (Figure 3). It can be seen that, as the strength of the field increases from 0.01 T, the same magnetic field strength of a strong refrigerator magnet [12], to 0.2 T, the x-direction displacement of the loaded node (node 4) decreased by 95%. The spring stiffness, or the slope of the lines in Figure 3, increased by a factor of 2. This means that the local structure stiffening of smart materials impregnated with MR fluid would increase bulk stiffening of the chamber walls.

To validate this approach, truss structures are created in

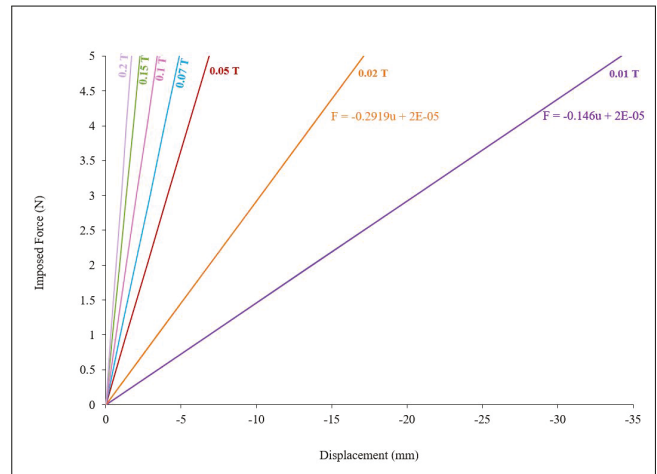


Fig. 3: Displacement of support node, node 4, of simple truss under various loading with increasing magnetic field

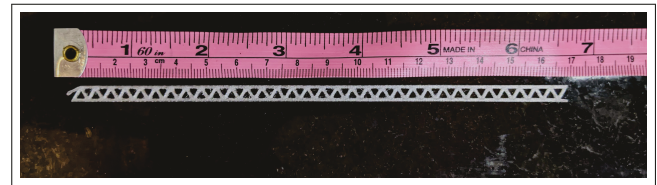


Fig. 4: 3-D printed truss

3-D modeling software and printed using an Ultimaker 3-Extended 3-D printer. Figure 4 is representative of the truss used to create MR fluid channels. The units of the truss can be repeated to customize it to the necessary length dependent on the application. To create channels in an elastomeric material, like that of Smooth-On Dragon Skin 10 (DS10) or Smooth-On Dragon Skin 30 (DS30), the 3-D printed material, polylactic acid (PLA), will be depolymerized while embedded in the cured rubber. The depolymerization process creates the channels by which MR fluid may be injected. An example of a truss structure prior to depolymerization is shown in Figure 5. Previously, this method of creating hollow networks within a matrix has only been done in rigid epoxy substrates. Utilizing the Esser-Kahn method [13] for thermal depolymerization of PLA, the PLA will be treated with a catalyst to promote exodus from the silicone matrix by lowering the required temperature threshold for this process.

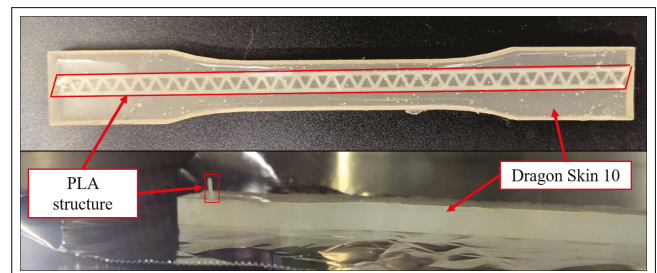


Fig. 5: PLA truss embedded in silicone tensile specimen

III. WORKSPACE CHANGES BY STIFFNESS MODULATION

The truss simulation indicates that it is possible to substantially modify the stiffness of individual regions of the chamber wall by varying the magnetic field applied to the MR fluid in the channels. We wish to know what effect the applied magnetic field will have on the robot's reach when pressurized. With this goal in mind, we conducted an experiment to evaluate the accessible workspace for a robot with patches of differing stiffness that approximate this effect.

Much work has been done with straight arms [14], but an initially straight fabric reinforced chamber, would only yield a planar motion for the base arm with a uniform silicone composition. It was deemed desirable for the control arm to have a 3-dimensional motion in order for the changes in wall stiffness to have the most visible effect on the later arms. For this purpose, a curved undeformed geometry was chosen as shown in Figure 1. The base arm with no changes to wall stiffness yielded a motion similar to tracing out the edge of half of a hyperbolic paraboloid.

We evaluated the effect stiffness changes to the walls would have on the robot's trajectory as it is inflated with multiple robots. Each one had a strip of rubber of different Shore Hardness from that of the rest of its chamber in some location. This was done in order to gain qualitative insight into how changes in wall stiffness affect the arm's motion and change its workspace and to work on the testing of our model [15]. The robots tested included DS30 chambers with strips of DS10 at various locations, and DS10 chambers with strips of DS30 at various locations. The Ruess calculation, $\text{Log}_{10}E = 0.0235S - 0.6403$, correlates Shore Hardness, S , to the elastic modulus, E . The equation predicts a threefold elastic modulus increase from DS10 to DS30. As mentioned in the previous section, our initial truss configuration indicated the active material could alter stiffness by a factor of 2 with future configurations likely to increase this factor.

A. Manufacturing

Curved, three-part arm molds were 3D printed, as were molds that would form strips that curve with the geometry of the arm (Figure 6). The arm mold has pin holes to align the core and prevent the creation of large variations in wall thickness. These methods loosely follow the work of Marchese et al. and Takayama et al. [7], [16]. They and the strip molds that clamp in a vertical orientation also have small silicone reservoirs that are filled after the mold is clamped to ensure voids do not form at the top of the molds as silicone settles (Figure 7). After some testing of different wall thicknesses, all molds create arms or additions with a 2 mm wall thickness. Other testing revealed that pre-cured silicone bonds to silicone that was poured later regardless of differences in Shore Hardness. This is the operating principle behind making composite arms (composite here meaning the use of two silicones with differing elasticities).

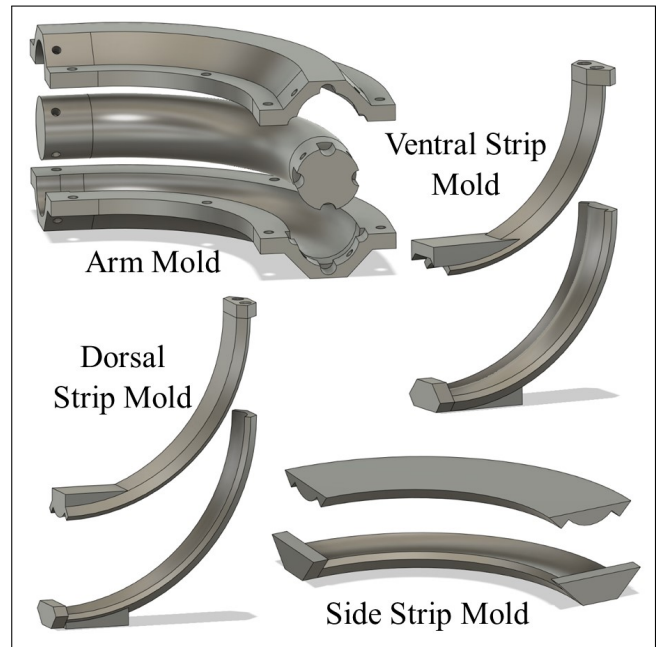


Fig. 6: Arm and Strip Molds

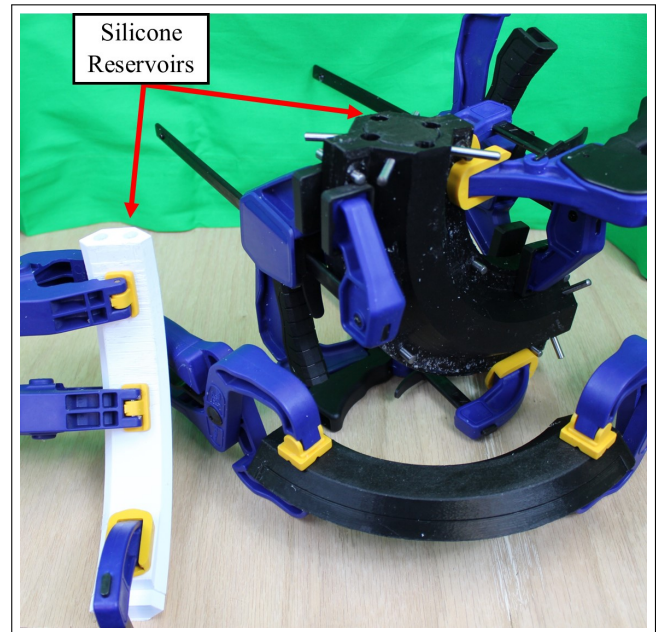


Fig. 7: Clamped Molds

When preparing silicone for molding (Smooth-On Dragon Skin 10 or 30, slow cure), we found that allowing it to cure for 35 minutes in a vacuum chamber under -94 kPa before pouring yielded the best results. This both removed air from the silicone and allowed it to cure to a sufficient viscosity that it would not leak out of the molds. We also found that it was best to encase the fabric in silicone before putting it in the arm mold. This was because the fabric had a tendency

to float away from the desired location if it was not adhered to the wall of the arm mold. A silicone encased fabric strip could be glued to the right location on the wall or core of the arm mold prior to pouring, which prevented movement.

For each arm, a strip of radial fabric is cut to fit within the side strip mold (bottom right of Figure 6). Silicone is then prepared, as previously described, and poured over into the side strip mold. The fabric is pressed into silicone and more silicone is poured over the fabric. Finally, the mold is closed and clamped (see Figure 7). Strip additions are created in a similar manner. Silicone is poured into both halves of the mold, which are then assembled and clamped together.

Once all additions have been cured, removed, and excess silicone (either from the seams or the reservoirs), has been cut away; an arm can be molded. As mentioned, additions tend to float away from their desired location before the silicone has set. Therefore, they should be adhered to the wall or core of the arm mold as in Figure 8 (we found Sil-Poxy to work best). Once the adhesive has cured, silicone is poured into the bottom half of the arm mold (either side works). The core is pressed into the silicone and additional silicone is poured over the core. Finally, the other half of the mold is put in place and the mold is pinned and clamped in the orientation shown in the bottom picture of Figure 6. Excess silicone is squeezed into the reservoirs in the manner of Takayama et al., preventing voids in the mold [16].



Fig. 8: Arm Molding Preparation

Strips of DS10 were embedded in arms made of DS30 in different locations and vice versa. The following naming convention was chosen (Figure 9). The fabric for each arm ran along the left side. Arms pairs (DS10 strips within 30 and 30 within 10) were made with a silicone strip on the right side, opposite the fabric. This was done with full strips (0 to 90 degrees), half-strips on each end (0 to 45 and 45 to 90 degrees), and half-strips centered (22.5 to 67.5 degrees). Some of the same permutation pairs were made for the dorsal and ventral. A table of tested arms is provided (see Table I).

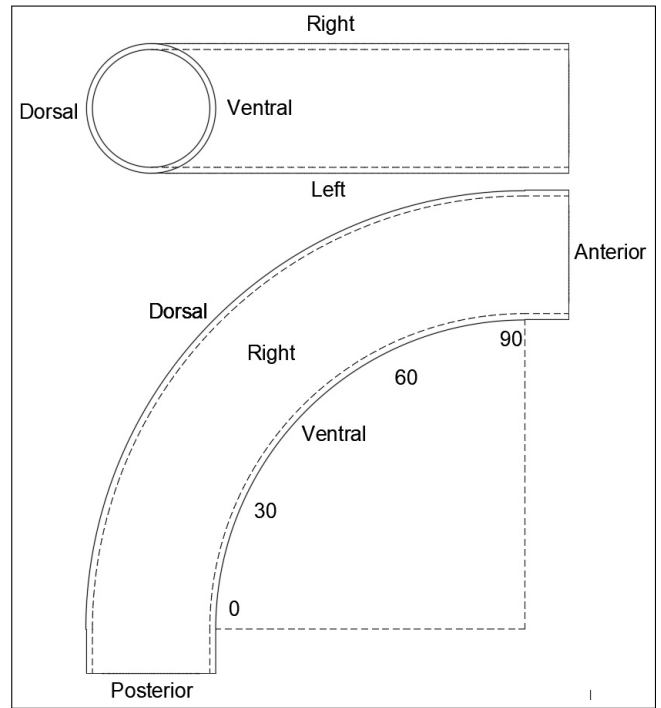


Fig. 9: Arm Morphology Convention

TABLE I: Arm Variations Tested

	30 Strip in 10	10 Strip in 30
0-90 deg	Right, Dorsal, Anterior	Right, Dorsal
0-45/45-90 deg	Right, Dorsal	Right
22.5-67.5 deg	Right	Right

B. Position Tracking with Inflation

Once the robot arms had cured and were removed from the molds, the workspace of each of these arms was evaluated. The workspace of an individual arm is defined as the volumetric space which any part of that arm could touch. This is also the volume that is created by sweeping the original volume of the arm through space. The arms were inflated manually from a pressure reservoir. The maximum arm pressure varied between the predominately DS10 and predominately DS30 arm families. The DS10 arms could not withstand the pressure that the DS30 arms could even when the DS30 arms had DS10 additions. While this trend held true, each arm's maximum pressure was determined visually during testing. The Polhemus Liberty 3D tracking system was used to capture the motion of markers placed at various locations on each arm. The sensor placement can be seen in Figure 1 (though some sensors were removed from the data in some tests due to an equipment malfunction). For a soft robot, any portion of the arm's surface can be used to bump, push, and scrape its environment. This is why the entire arm is tracked rather than just the end effector. In addition to these sensors, a reference sensor was attached to the fixed base of each arm. The sensors were placed to minimize the tracking of radial expansion and focus on the motion path

of the arm. This placement does mean that the point cloud data does not capture the dorsal side or the side opposite the fabric and therefore underestimates the workspace by a small amount.

Once the point cloud data was collected for all arms, the convex hull of those points was calculated (Figure 10). The colored lines in this figure represent the end effector sensor's path for a few selected tests. The blue smaller hull within the larger cyan hull shows the volume swept out by the arm of uniform rubber composition. A model of the robot in its undeformed state has been placed within the larger hull to give a better idea of the scale and orientation of the hull. The convex hull overestimates the workspace anywhere that the sensors trace out a concave area. However, an examination of the workspace shows that all sensor paths are convex. While some small concave overestimation areas may exist, this workspace provides a tight upper bound for the robot's reach.

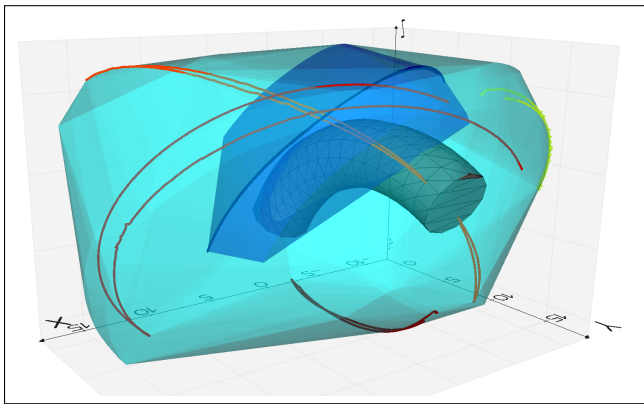


Fig. 10: Collated Data Convex Hull

The composite arms differ markedly in movement compared to an arm of uniform rubber composition (e.g. DS10 only). Figure 11 shows the final state of the arm made uniformly of DS10 vs one made primarily of DS10 with a DS30 strip along the entire dorsal side. As previously mentioned, the workspace for a soft robot is more than just the surface created by the sweeping of the end effector. The workspace shown represents the volume of the arm swept through space. Because of this, even the motion of one arm will have a volume and not just a surface area. The base arm had a workspace volume of 866 cm^3 , while the workspace of all arms combined was $5,503 \text{ cm}^3$. This means that an arm with walls embedded with smart materials will have a much larger workspace than one without. In fact, many more configurations could be tested and would likely discover other regions of the potential workspace beyond those found in these tests.

An interesting observation made during these tests was that the two silicones each had a narrow range of pressures at which they would deform. Each would exhibit little strain before reaching their “operating range”. They would then strain suddenly through there motion path. After which, they would strain harden and deform no further despite increased

pressure. DS10 started deforming in the 1-2 psi range, while DS30 showed almost no deformation until the 3-4 psi range. This meant that a DS10 strip within a DS30 arm would move through almost its entire deformation range before the DS30 had deformed much at all. Conversely, a DS30 strip behaved almost completely inelastically within the DS10 arm housing as it deformed. Despite this difference in operating pressure, the overall deformation between the two arm families of differing rigidity was similar. This means it may be possible for arms with multiple varying stiffness patches embedded in them to deform in radically different ways at different pressures even without controllable stiffness.

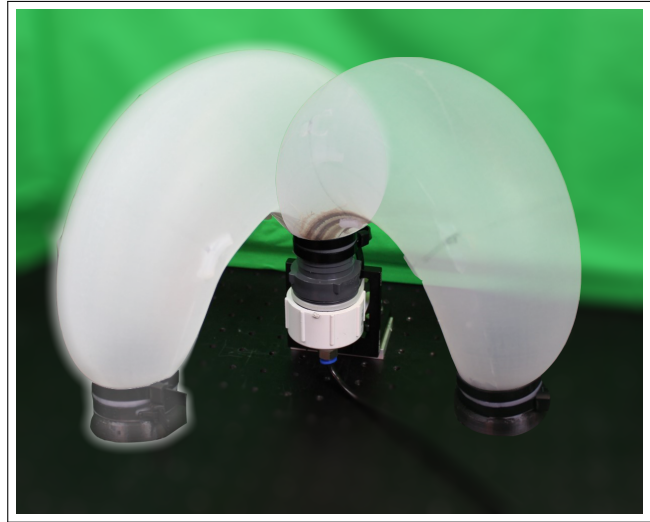


Fig. 11: Uniform DS10 (Right) vs. DS10 with DS30 Dorsal Strip (Left): Final States

IV. CONCLUSIONS

In this study, we demonstrated that changes to wall stiffness in a single-chambered, fabric reinforced arm dramatically alter its motion path and increase its workspace. The integration of patches of silicone with differing elastic moduli in the arm's wall yielded a workspace that was over six times the volume of the uniform arm. A model of a simple planar magnetically responsive truss channel indicates that activation of these MR channels could increase the stiffness of the active material twofold. This suggests that integration of these MR materials in the chamber walls could allow the robot to reach a similar-sized region under a changing magnetic field. More work in this area will likely increase this factor by optimization of the truss structural geometry.

Continuing this study, we will use depolymerized 3-D printed preforms to create channels in silicone specimens that will be filled with MR fluid. Tensile testing of the proposed smart material will be modified to include a range of magnetic field strengths. The modified testing will validate the range of stiffness for which the MR infused silicone can modulate. Next, experimental confirmation of stiffness patch testing will be performed by embedding the same MR fluid-filled channels into the arms of the robot. These MR fluid arms will be tested by altering magnetic fields around

them to evaluate the produced workspace. While the work to incorporate the MR fluid channels into an arm is being done, there are many untested patch configurations to be explored. It is likely that a torsional moment induced by stiffness patches could increase the workspace even further. Tests using helical patches or multiple patches in different positions may accomplish this. These tests would provide further insight into what changes different activations of the MR fluid can cause. Beyond the creation and workspace testing of these arms, dexterity, force, and other basic robot tests will be performed. These will be beneficial in comparing this movement modality to other soft robots and traditional robots. Specifically, a demonstration involving closely placed obstacles that require a tight turning radius would test the usefulness of magnetorheologically induced locomotion.

A single-chambered robot with the ability to achieve complex motion by rapidly modulating its wall stiffness allows a one-chambered robot to have multiple degrees of freedom. While multi-chambered robots are limited to the motion allowed by the configuration of their chambers, magnetically activated motion gives many more movement options. This is also done in a much more useful timescale than thermally activated wall stiffness modulation methods like wax. An appendage utilizing our proposed smart material would not be limited to a specific motion type. It could therefore accomplish a wide range of tasks and do so in a reasonable amount of time.

REFERENCES

- [1] M. Manti, V. Cacucciolo, and M. Cianchetti, "Stiffening in soft robotics: A review of the state of the art," *IEEE Robotics and Automation Magazine*, 2016.
- [2] R. F. Shepherd, F. Ilievski, W. Choi, S. A. Morin, A. A. Stokes, A. D. Mazzeo, X. Chen, M. Wang, and G. M. Whitesides, "Multigait soft robot," *Proceedings of the National Academy of Sciences of the United States of America*, vol. 108, no. 51, pp. 20400–20403, 2011.
- [3] F. Ilievski, A. D. Mazzeo, R. F. Shepherd, X. Chen, and G. M. Whitesides, "Soft robotics for chemists," *Angewandte Chemie - International Edition*, vol. 50, no. 8, pp. 1890–1895, 2011.
- [4] K. McDonald, A. Rendos, S. Woodman, K. A. Brown, and T. Ranzani, "Magnetorheological Fluid-Based Flow Control for Soft Robots," *Advanced Intelligent Systems*, p. 2000139, sep 2020.
- [5] B. Hansen, "Photographic evidence of a unique type of walking in deep-sea holothurians," *Deep-Sea Research and Oceanographic Abstracts*, vol. 19, no. 6, pp. 461–463, 1972.
- [6] K. C. Galloway, P. Polygerinos, C. J. Walsh, and R. J. Wood, "Mechanically programmable bend radius for fiber-reinforced soft actuators," *2013 16th International Conference on Advanced Robotics, ICAR 2013*, 2013.
- [7] A. D. Marchese, R. K. Katzschmann, and D. Rus, "A recipe for soft fluidic elastomer robots," *Soft Robotics*, vol. 2, pp. 7–25, mar 2015.
- [8] M. R. Jolly, J. D. Carlson, and B. C. Muñoz, "A model of the behaviour of magnetorheological materials," *Smart Materials and Structures*, vol. 5, pp. 607–614, oct 1996.
- [9] J. A. Jackson, M. C. Messner, N. A. Dudukovic, W. L. Smith, L. Bekker, B. Moran, A. M. Golobic, A. J. Pascall, E. B. Duoss, K. J. Loh, and C. M. Spadaccini, "Field responsive mechanical metamaterials," *Science Advances*, 2018.
- [10] N. G. Cheng, A. Gopinath, L. Wang, K. Iagnemma, and A. E. Hosoi, "Thermally tunable, self-healing composites for soft robotic applications," *Macromolecular Materials and Engineering*, vol. 299, no. 11, pp. 1279–1284, 2014.
- [11] X. Zheng, H. Lee, T. H. Weisgraber, M. Shusteff, J. DeOtte, E. B. Duoss, J. D. Kuntz, M. M. Biener, Q. Ge, J. A. Jackson, S. O. Kucheyev, N. X. Fang, and C. M. Spadaccini, "Ultralight, ultrastiff mechanical metamaterials," *Science*, 2014.
- [12] "Tesla - MagLab."
- [13] A. P. Esser-Kahn, P. R. Thakre, H. Dong, J. F. Patrick, V. K. Vlasko-Vlasov, N. R. Sottos, J. S. Moore, and S. R. White, "Three-dimensional microvascular fiber-reinforced composites," *Advanced Materials*, 2011.
- [14] B. Shih, D. Drotman, C. Christianson, Z. Huo, R. White, H. I. Christensen, and M. T. Tolley, "Custom soft robotic gripper sensor skins for haptic object visualization," *IEEE International Conference on Intelligent Robots and Systems*, vol. 2017-Septe, pp. 494–501, 2017.
- [15] J. A. Schultz, H. Sanders, P. D. H. Bui, M. W. Keller, and M. Killpack, "Representing fabric-reinforced inflatable robots by discs and threads," in *International Mechatronics Conference and Workshops*, (Oklahoma City, USA), p. to appear, October 2020.
- [16] T. Takayama, H. Takeshima, T. Hori, and T. Omata, "A twisted bundled tube locomotive device proposed for in-pipe mobile robot," *IEEE/ASME Transactions on Mechatronics*, vol. 20, pp. 2915–2923, Dec 2015.